Received: 30 November 2018 | Revised: 7 January 2019 | Accepted: 8 January 2019

DOI: 10.1002/mrm.27675

FULL PAPER

Magnetic Resonance in Medicine

Accuracy and precision of electrical permittivity mapping at 3T: the impact of three B_1^+ mapping techniques

Soraya Gavazzi[1] | **Cornelis A. T. van den Berg**[1,2] | **Alessandro Sbrizzi**[2] | **H. Petra Kok**[3] | **Lukas J. A. Stalpers**[3] | **Jan J.W. Lagendijk**[1] | **Hans Crezee**[3] | **Astrid L. H. M. W. van Lier**[1]

[1]Department of Radiotherapy, University Medical Center Utrecht, Utrecht, The Netherlands

[2]Center for Image Sciences, University Medical Center Utrecht, Utrecht, The Netherlands

[3]Department of Radiation Oncology, Amsterdam UMC, University of Amsterdam, Amsterdam, The Netherlands

Correspondence
Soraya Gavazzi, Department of Radiotherapy, University Medical Center Utrecht, P.O. Box 85500, 3508 GA Utrecht, The Netherlands.
Email: s.gavazzi@umcutrecht.nl

Funding information
Dutch Cancer Society (KWF; project UVA 2014-7197)

Purpose: To investigate the sequence-specific impact of B_1^+ amplitude mapping on the accuracy and precision of permittivity reconstruction at 3T in the pelvic region.

Methods: B_1^+ maps obtained with actual flip angle imaging (AFI), Bloch–Siegert (BS), and dual refocusing echo acquisition mode (DREAM) sequences, set to a clinically feasible scan time of 5 minutes, were compared in terms of accuracy and precision with electromagnetic and Bloch simulations and MR measurements. Permittivity maps were reconstructed based on these B_1^+ maps with Helmholtz-based electrical properties tomography. Accuracy and precision in permittivity were assessed. A 2-compartment phantom with properties and size similar to the human pelvis was used for both simulations and measurements. Measurements were also performed on a female volunteer's pelvis.

Results: Accuracy was evaluated with noiseless simulations on the phantom. The maximum B_1^+ bias relative to the true B_1^+ distribution was 1% for AFI and BS and 6% to 15% for DREAM. This caused an average permittivity bias relative to the true permittivity of 7% to 20% for AFI and BS and 12% to 35% for DREAM. Precision was assessed in MR experiments. The lowest standard deviation in permittivity, found in the phantom for BS, measured 22.4 relative units and corresponded to a standard deviation in B_1^+ of 0.2% of the B_1^+ average value. As regards B_1^+ precision, in vivo and phantom measurements were comparable.

Conclusions: Our simulation framework quantitatively predicts the different impact of B_1^+ mapping techniques on permittivity reconstruction and shows high sensitivity of permittivity reconstructions to sequence-specific bias and noise perturbation in the B_1^+ map. These findings are supported by the experimental results.

KEYWORDS
accuracy and precision, B_1 mapping, Helmholtz-based EPT, permittivity mapping

[Correction added after online publication 13 March 2019. The authors have corrected minor typographical and grammar issues throughout the article.]

1 | INTRODUCTION

Knowledge of electrical tissue properties is necessary to build patient-specific electromagnetic (EM) models, which are fundamental for radiofrequency (RF) safety[1,2] and treatment planning for therapeutic heating of malignant tissues using RF or microwave antennas.[3-7] For example, patient-specific electrical properties may be used as input for planning in locoregional hyperthermia treatment of patients with pelvic tumors (e.g., cervix) with phased arrays of 70-130 MHz antennas.[6,7] In this frequency range, however, electrical properties might vary (e.g., the permittivity variation is 11% in muscle and 15% in the cervix) because of their dispersive nature[8]; thus, electrical properties should be characterized at a frequency near the frequency used for treatment in order to improve the reliability of treatment planning. Moreover, a great body of literature has shown differences between the electrical properties of healthy and malignant human tissues[9-17]; such differences could potentially be exploited for diagnostic purposes. Therefore, measuring electrical tissue properties, being permittivity (ε_r) and conductivity (σ), has since long been an important research question.[8,18-20]

A relatively recent MR-based technique, called electrical properties tomography (EPT),[1,21,22] extracts noninvasively the in vivo electrical properties of tissues from the spatial modulation of the circularly polarized component (B_1^+) of the transverse RF transmit field, which is responsible for spin excitation. This spatial modulation in the complex B_1^+ field is determined by induced conduction and displacement currents (which are governed by tissue conductivity and permittivity distributions), the applied RF frequency (e.g., 128 MHz at 3T proton imaging), and the incident RF field.[23-25] To the leading order, the permittivity is encoded in the amplitude of the B_1^+ field ($|B_1^+|$), whereas the conductivity is reflected in the phase of such field.[25-28] Therefore, measuring accurate and precise B_1^+ amplitude and phase maps is essential in EPT, given that the quality of these maps intrinsically influences the quality of both property estimates. Indeed, Lee et al theoretically demonstrated that the precision of permittivity and conductivity reconstructed with a Helmholtz-based algorithm depends linearly on the precision of B_1^+ amplitude (or $SNR_{B_1^+}$) and phase maps, respectively.[29] Seemingly, the accuracy of both properties is expected to be proportional to the accuracy of the measured B_1^+ amplitude and phase maps,[21,30] although it has never been verified.

To date, several techniques for B_1^+ field mapping have been used in EPT studies (e.g., standard spin echo, gradient echo, and balanced steady-state free precession for phase mapping and actual flip angle imaging (AFI)[31] and double-angle methods[32] for $|B_1^+|$ mapping) and numerous algorithms have been proposed to disentangle both properties from the B_1^+ field.[1,27-29,33-45] Based on measured field maps, in vivo conductivity maps have been derived (e.g., see previous works[1,27,28,33,37,44,45]) and also preliminarily tested for clinical oncologic applications, for example, in brain,[17,46-48] breast,[16,49] and uterine cervix.[50] At the same time, a few studies have reported in vivo permittivity maps,[27,37,51,52] but no study has exploited permittivity maps in clinical scenarios. Regardless of the chosen EPT reconstruction algorithm, the precision of these permittivity maps was poorer than that of conductivity images. These inferior results were attributed to higher noise levels in experimental $|B_1^+|$ maps.[27,51,52]

The underlying precision of B_1^+ amplitude and phase maps is dissimilar because both maps are measured independently and differently. The B_1^+ phase distribution is typically approximated with the phase image acquired with standard MR sequences. Thus, its precision is linearly proportional to the signal-to-noise ratio (SNR) of the MR image.[53] On the other hand, the $|B_1^+|$ is mapped with dedicated B_1^+ mapping sequences (e.g., see previous works[31,32,54-56]). These sequences utilize a model describing the sequence-specific B_1^+ encoding mechanism to derive the $|B_1^+|$ information from acquired MR images. This model regulates the noise propagation that leads to finite precision in the B_1^+ map. Moreover, the B_1^+ encoding model, which normally relies on approximations or assumptions, might degrade the accuracy of the $|B_1^+|$ calculation and therefore bias the estimated $|B_1^+|$ distribution.

B_1^+ mapping sequences that share similar encoding mechanisms (e.g., the double-angle and AFI-based techniques) are expected to have comparable accuracy and precision in the $|B_1^+|$ and consequently similar influence on the permittivity. However, although the accuracy and precision of $|B_1^+|$ maps obtained with some B_1^+ mapping sequences have already been assessed in studies unrelated to EPT,[57-60] the impact of $|B_1^+|$ acquisition on accuracy and precision of the permittivity map remains still unknown.

Hence, in this study, we investigate the specific impact of the $|B_1^+|$ sequence on permittivity mapping. To this aim, we examined three commonly commercially available sequences (namely, AFI,[31] Bloch–Siegert [BS] shift,[54] and dual refocusing echo acquisition mode [DREAM][55]), which have distinct B_1^+ encoding mechanisms. Clinically acceptable scanning times are essential, and therefore the three B_1^+ techniques were set to image the $|B_1^+|$ in the pelvic region within 5 minutes. B_1^+ maps of the pelvic region at 3T were of interest to estimate permittivity at ~128 MHz, which falls within the frequency range (70–130 MHz) applied for locoregional hyperthermia treatments of cervical cancers.[61] By designing a methodological framework consisting of (1) mathematical models, (2) numerical simulations, and (3) MR measurements that take the sequence-specific generation of the $|B_1^+|$ distribution into account, we quantified to what extent the quality of different B_1^+ amplitude maps affects accuracy and precision of the resulting permittivity maps. Comparing these permittivity maps highlighted the impact of sequence-specific $|B_1^+|$ accuracy and precision on the permittivity.

2 | METHODS

Phantom MR simulations and measurements and in vivo measurements were performed with AFI, BS, and DREAM techniques, which were set to map B_1^+ amplitude distribution in the pelvic region within 5 minutes at 3T. From these $|B_1^+|$ data, permittivity maps were obtained. Figure 1 illustrates the complete workflow of our study. Subsequently, accuracy and precision of both $|B_1^+|$ and permittivity maps have been evaluated and compared. Hereafter, we define *accuracy* as the bias caused by model imperfections between the estimate of the quantity and the true quantity (in our case, this quantity could be B_1^+ amplitude or the permittivity), in the absence of noise. The *precision*, instead, is inversely related to the standard deviation (std) of the estimate (i.e., precision = $(\text{std})^{-2}$) and generally reflects the propagation of noise. Moreover, we will use the term "B_1^+ map" to refer to the B_1^+ amplitude map, unless explicitly stated otherwise.

2.1 | Phantom and in vivo

For simulations and measurements, a pelvic-sized phantom was used consisting of 2 compartments[62]: an elliptically shaped cylinder and an inner sphere (Figure 2). The outer cylinder was made of poly(methyl methacrylate). The inner sphere was ~7.5 mm thick and was made of polystyrene. Phantom composition, dielectric properties, and relaxation times are listed in Table 1. Dielectric properties of the solutions contained in the inner and outer compartments were measured with a dielectric probe (85070E; Agilent Technologies, Santa Clara, CA) and matched those of the uterus and the average female pelvis, respectively, based on literature values.[8] Measurements were also conducted on the pelvis of a female volunteer (whose written informed consent was obtained).

2.2 | MR experiments

All experiments were performed on a 3T scanner (Ingenia; Philips Healthcare, Best, Netherlands), using a 28-channel torso array for reception. For all three techniques, a 3D acquisition was chosen because of its inherently higher SNR compared to 2D acquisition, essential for EPT. For each sequence, settings were chosen to achieve a scan length of 5 minutes for a field of view (FOV) = 480 × 260 × 80 mm^3 with voxel size 2.5 × 2.5 × 5 mm^3 (transverse orientation; Table 2). A multislice spin echo sequence was used to map the transceive phase. To obtain an eddy-current–free transceive phase map, 2 identical spin echo scans with opposed gradient polarity were acquired.[1] For all MR scans, the vendor-specific

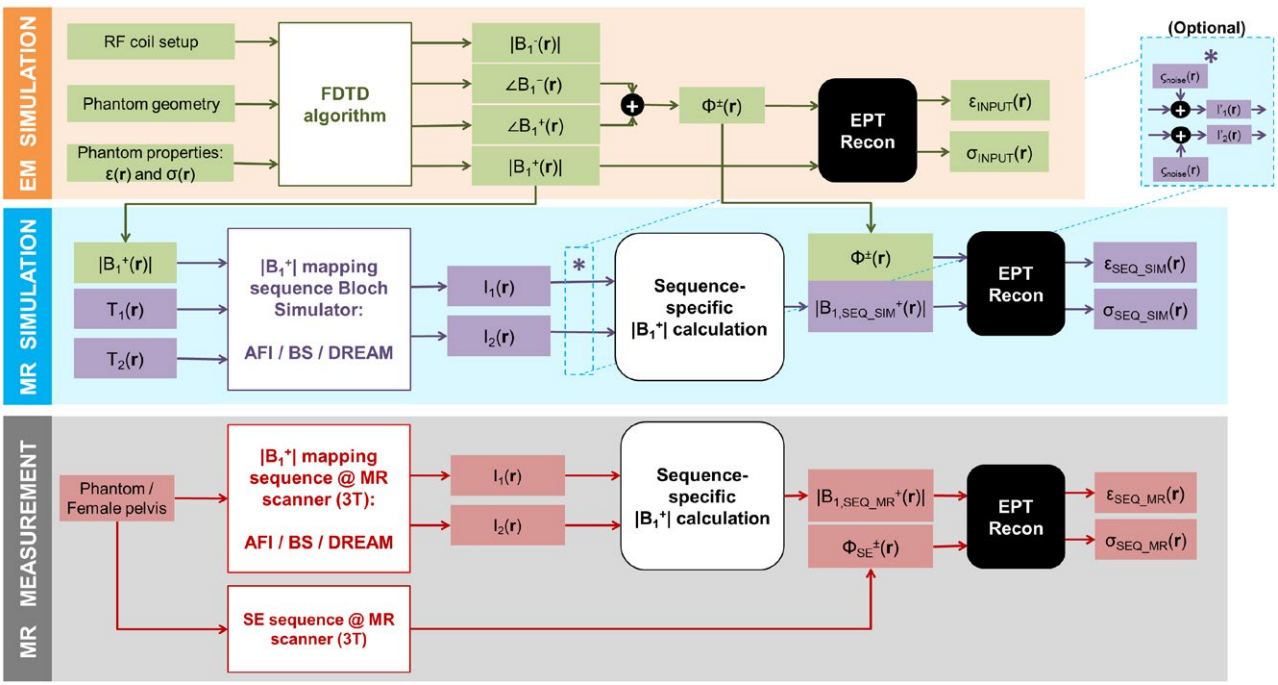

FIGURE 1 From B_1^+ generation to permittivity (ε_r) reconstruction: workflow of our study, consisting of an EM simulation, MR simulations, and MR measurements on a phantom and in vivo MR measurements on a female pelvis. For the MR simulations, Gaussian noise ς_{noise} could be optionally added separately to both real and imaginary parts of the signals I_1 and I_2 (denoted by the asterisk and the block "Optional"). In the MR measurements, a separate SE sequence was performed to retrieve a transceive phase map ($\Phi_{SE}^{\pm}$) needed for EPT reconstruction. The sequence-specific calculations were performed according to the formulas reported in the Appendix. The subscript "SEQ" refers to any sequence among AFI, BS, and DREAM

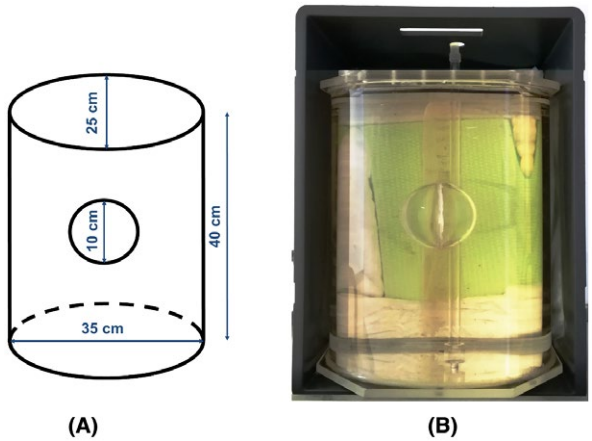

FIGURE 2 Phantom used for simulations and measurements. A, Schematic view of the phantom, with its dimensions. B, Picture of the phantom

TABLE 1 Phantom characteristics

	Inner compartment	Outer compartment
Composition	6 g/L NaCl	Ethylene glycol + 64 g/L NaCl
ε_r (rel. units)[a]	80	36
σ (Sm^{-1})	0.99	0.47
T_1 (ms)[b]	3929	500
T_2 (ms)	433	74

[a]Values for permittivity ε_r and conductivity σ were measured with a dielectric probe (85070E; Agilent Technologies, Santa Clara, CA) from samples of both solutions.
[b]T_1 and T_2 values are average values taken from T_1 and T_2 maps measured with a vendor-specific "mix-TSE" sequence (single slice, isotropic voxel size = 5 mm).

CLEAR option was enabled.[63] With CLEAR, the combined transceive phase of the body coil and the torso array is converted to the transceive phase of the body coil only.

2.3 | MR simulations

The complex B_1^+ field pattern in the phantom, as generated by a 16-rod birdcage RF coil, was simulated using an in-house developed FDTD (finite-difference-time-domain) algorithm.[64] The coil was tuned at 128 MHz (3T) and driven in quadrature mode. A resolution of $2.5 \times 2.5 \times 5$ mm^3 was used for the simulation. The resulting components of the magnetic field were combined to obtain the complex magnetic transmit field (B_1^+) and complex magnetic receive field (B_1^-; Figure 1).

Subsequently, the MR experiment for each B_1^+ mapping sequence was emulated in Matlab (R2015a; The MathWorks, Inc., Natick, MA) by using a Bloch simulator.[65] Input for these simulations were the geometry of the phantom model, the B_1^+ amplitude map from the FDTD simulation (also called "input B_1^+" in this study), and T_1 and T_2 values (see Figure 1 and Table 1). The input B_1^+ map was normalized to the average $|B_1^+|$ value in the central slice. Therefore, all values relating to B_1^+ are reported as relative units.

Rectangular-shaped RF excitation pulses were used, except for the off-resonant Fermi pulse in BS. All pulses were set to achieve an average flip angle equal to the chosen nominal flip angle in the experiments (Table 2) and were scaled by the input transmit field. Imaging gradients were also approximated as rectangular blocks. Furthermore, we assumed ideal spoiling of the transverse magnetization at the end of each TR. Two different simulation approaches were used according to the acquisition regime of each sequence. For the steady-state sequences (AFI and BS), the voxel signal corresponded to the signal value at TE (i.e., the value at the center of k-space). Differently, to mimic the multishot imaging modality of DREAM, the full readout and phase-encoding gradient schemes were implemented. Thus, the full k-space was collected and then Fourier transformed into the image domain to obtain the MR image.

For each sequence, the output of each simulation was two MR images (I_1 and I_2; Figure 1). These images were combined to form the B_1^+ map according to the sequence-specific B_1^+ encoding mechanism, as outlined in the Appendix. To simulate the full phantom volume, the sequence simulation was looped over all slices.

2.4 | Permittivity reconstruction

Permittivity maps were reconstructed with a Helmholtz-based EPT method. This method is based on a finite-difference Laplacian implementation: specifically, the noise-robust kernel was used for the Laplacian operator.[28] The kernel size was $7 \times 7 \times 5$ voxels.

The EPT reconstruction requires the complex B_1^+ field as input data (i.e., both the amplitude and phase distribution maps). Because the phase of the transmit field (ϕ^+) is not directly measurable in MR, the transceive phase assumption[26] was used. The transceive phase assumption approximates the B_1^+ phase as half of the *transceive phase* ($\phi^\pm$), namely the sum of B_1^+ and B_1^- phases. Van Lier et al[28] and Balidemaj et al[62] showed that this approximation introduced a minor phase error in both the brain at 7T and the pelvis at 3T.

We reconstructed permittivity maps based on complex B_1^+ data from both simulations and experiments. The B_1^+ amplitude map was derived from AFI, BS, and DREAM measurements or simulations. The transceive phase was derived from the spin-echo–based transceive phase map (measurements) and from the sum of B_1^+ and B_1^- phases obtained in the EM simulation (Figure 1). We also reconstructed the permittivity from the true "B_1^+" amplitude and transceive phase (i.e., the maps without influence of the B_1^+ mapping technique). We called this permittivity map "input permittivity." Note that

TABLE 2 Protocol parameter settings for both simulations and measurements

	AFI	BS	DREAM	SE[a]
FOV (mm^3)	480 × 260 × 80	480 × 260 × 80	480 × 260 × 80	480 × 260 × 80
Voxel size (mm^3)	2.5 × 2.5 × 5	2.5 × 2.5 × 5	2.5 × 2.5 × 5	2.5 × 2.5 × 5
Spatial encoding	3D	3D	3D	2D multislice
Imaging flip angle (°)	60	60	15	90
TE (ms)	2.5	12	TE_1/TE_2 = 2.1/4.6	6
TR (ms)	TR_1/TR_2 = 30/155	93	7.7	1000
Fast imaging mode	None	None	Ultrafast GRE, 2 shots	None
Sequence-specific options	N.A.	Fermi pulse angle: 725° Fermi pulse duration: 8 ms Fermi pulse offset frequency: 4 kHz K_{BS}: 90.2 rad/G^2	STE-first scheme STEAM flip angle: 40° STEAM slice thickness: 20 mm Shot interval length: 3900 ms	N.A.
Pixel BW (Hz)	409.8	479.4	790.5	586.5
NSA	1	1	2	1
Scan duration (min:sec)	5:00	5:02	5:05	7:06

Settings apply for both phantom and in vivo cases.
NSA = number of signal averages; N.A. = not applicable; GRE = gradient echo.
[a]The SE technique was used only for MR measurements to map the transceive phase. Its scan time duration refers to the time needed to acquire 2 identical SE scans with opposed gradient polarity (for compensation of eddy currents).

this input permittivity represents the best permittivity that could be obtained with the abovementioned reconstruction method.

2.5 | Effect of transceive phase assumption

To assess the impact of the transceive phase assumption on permittivity, we simulated two types of permittivity: the first permittivity was reconstructed from the B_1^+ amplitude map and the transceive phase map, and the second was based on the B_1^+ amplitude and phase maps.

2.6 | Region-of-interest delineation

For both measurements and simulations, two regions of interest (ROIs) corresponding to the two compartments were manually delineated. All ROI delineations did not include the boundary errors caused by Helmholtz-based EPT reconstruction. In vivo, three ROIs were defined corresponding to the whole pelvis, bladder, and fat tissues. These ROIs were based on thresholding on magnitude images followed by further erosion to exclude the aforementioned EPT boundary errors.

2.7 | Accuracy assessment

As there is no reference technique ("golden standard") for B_1^+ mapping in experiments, accuracy (bias) of B_1^+ was assessed on noiseless simulated B_1^+ maps of the phantom. The bias in the B_1^+ pattern was illustrated by an error map representing the difference between the sequence B_1^+ map and the true B_1^+ distribution. To evaluate the isolated impact of the sequence-specific B_1^+ bias on accuracy in permittivity, we first reconstructed the permittivity maps on the abovementioned simulated B_1^+ maps. Then, we calculated the permittivity error (i.e. bias) maps, namely difference maps between the sequence-based permittivity and input permittivity. Moreover, an average accuracy for permittivity was estimated in both phantom simulations and measurements by calculating permittivity mean values in the ROIs.

2.8 | Precision assessment

Because precision and std are inversely related, we will use the std of the quantity under consideration as a measure for its precision. To avoid confusion with the conductivity symbol, we will denote the std with "ς." Hence, we will indicate hereafter noise level, std in the B_1^+ amplitude, and std in permittivity with ς_{noise}, $\varsigma_{B_1^+}$, and $\varsigma_{\varepsilon_r}$ respectively.

An analytical expression for the std in the B_1^+ map, $\varsigma_{B_1^+}$, was determined with the law of error propagation[66] for each B_1^+ mapping sequence (see the Appendix for more details) and used to generate $\varsigma_{B_1^+}$ maps in measurements and simulations. As shown in the Appendix, $\varsigma_{B_1^+}$ depends on sequence settings, the magnitudes or phases of the original images I_1 and I_2, and their SNRs (SNR_1 and SNR_2). To obtain the $\varsigma_{B_1^+}$ map from measured data, SNR maps corresponding to the images I_1 and I_2 were calculated with Kellman's method.[67] Implementation of

Kellman's method was validated with the temporal SNR method (SNR_{mult} in an earlier work[68]) in previous experiments (not shown). For both phantom and in vivo experiments, mean and std values for $\varsigma_{B_1^+}$ were calculated in the respective aforementioned ROIs.

In MR simulations (phantom only), instead, the real and imaginary parts of the images I_1 and I_2 were corrupted independently with a Gaussian noise level ς_{noise}. Subsequently, fictitious SNR_1 and SNR_2 maps were generated from the ratio of the noiseless image amplitude maps and ς_{noise}. Finally, a single map for $\varsigma_{B_1^+}$ was obtained. This procedure was repeated by using a range of realistic noise levels common to each technique. For each sequence and ς_{noise}, the resulting simulated maps for SNR_1 (and SNR_2) and $\varsigma_{B_1^+}$ were then spatially averaged inside the phantom. With these average values we predicted the relationship between $\varsigma_{B_1^+}$ and the image SNRs for the three sequences.

To determine the effect of realistic B_1^+ precision on the reconstructed permittivity, we performed a Monte-Carlo–based simulation (1000 iterations). In this case, the noise level used to corrupt the images in each technique was chosen such that the simulated image SNRs approximated the sequence-specific experimental image SNRs. In each iteration, a B_1^+ map was retrieved from these noisy images and used to reconstruct the permittivity. Subsequently, the permittivity mean and std maps over all iterations were calculated and eventually averaged inside the ROIs.

The std in permittivity, $\varsigma_{\varepsilon_r}$, was calculated on measured permittivity data in the ROIs corresponding to both compartments. Permittivity precision was then correlated with the B_1^+ precision found experimentally in the phantom.

3 | RESULTS

3.1 | Simulation results

3.1.1 | Accuracy

Noiseless simulations showed that all the techniques were able to reveal the B_1^+ field in the phantom (Figure 3A). Although these maps appeared to have perfect resemblance with the input field, difference maps exposed the subtle sequence-specific errors (Figure 3B). The maximum relative accuracy (i.e., $bias_{B_1^+} = \left| \left(B^+_{1,sequence} - B^+_{1,input}\right) / \left(B^+_{1,input}\right) \right|$) was 0.2% for AFI, 0.3% for BS, and 6.1% for DREAM in the inner compartment. In the outer compartment, the maximum

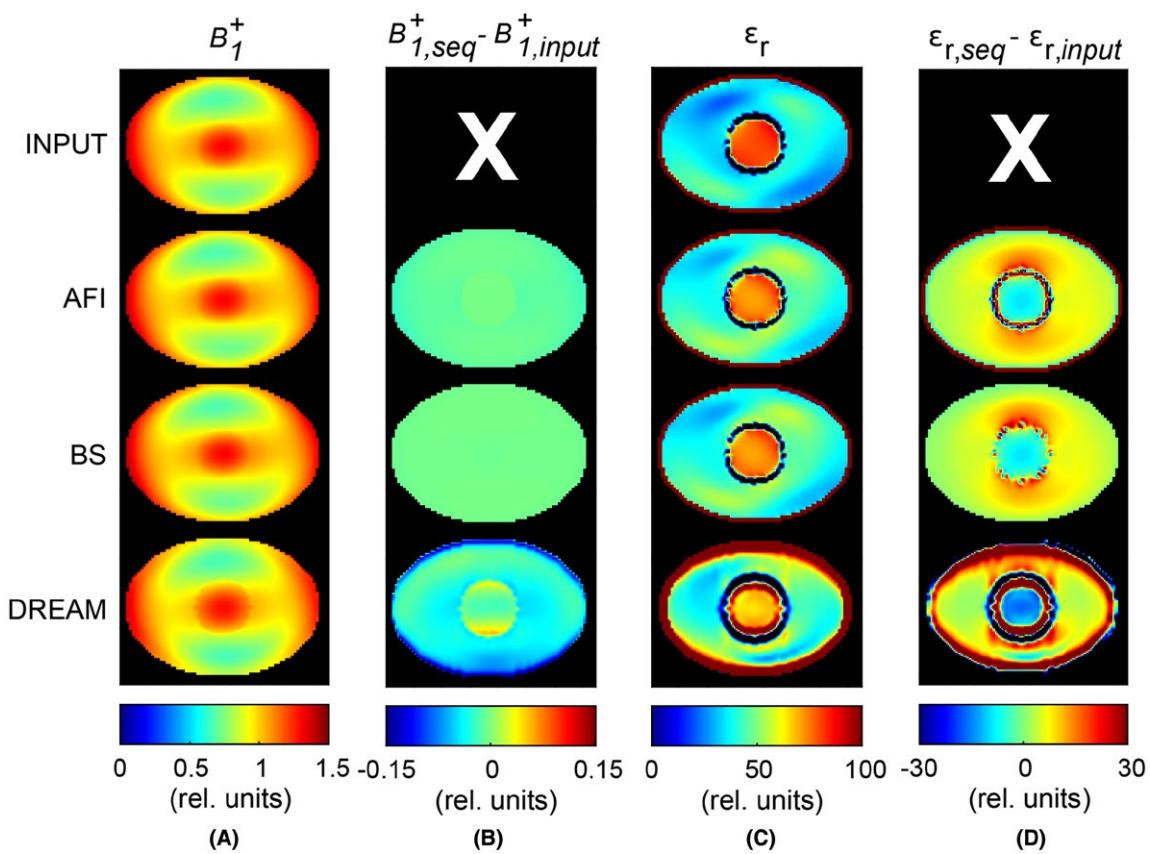

FIGURE 3 Phantom simulation study to assess the accuracy of both B_1^+ and ε_r, which were obtained with the EM simulation ("input," first row), AFI (second row), BS (third row), and DREAM (fourth row). No noise was added. A, B_1^+ maps. Values for the B_1^+ maps were normalized to the average value in the central slice. B, Map of the error in B_1^+ ($B^+{}_{1,sequence} - B^+{}_{1,input}$). C, Permittivity maps, which were reconstructed from the maps shown in (A) and the simulated transceive phase. D, Map of the error in ε_r ($\varepsilon_{r,sequence} - \varepsilon_{r,input}$). Note that the input permittivity ($\varepsilon_{r,input}$) accounts for the transceive phase assumption and is therefore the best permittivity that can be obtained with this EPT reconstruction method

relative accuracy was 1.5% for AFI, 0.3% for BS, and 15.4% for DREAM. Figure 3C depicts the permittivity maps reconstructed on these sequence-specific B_1^+ maps and the permittivity reconstructed on the input B_1^+, dubbed "input permittivity." For all these cases, the transceive phase obtained from the EM simulation was used together with the B_1^+ amplitude. The difference between the *sequence-specific* and *input* permittivity is reported in Figure 3D. This difference revealed the inaccuracies introduced by the B_1^+ mapping technique. The seemingly small bias in B_1^+ obtained with AFI and BS led to substantial errors in the permittivity maps. In the inner compartment, the relative bias for the permittivity (defined as $bias_{\varepsilon_r} = |\left(\varepsilon_{r,sequence} - \varepsilon_{r,input}\right) / \left(\varepsilon_{r,input}\right)|$) was, on average, 7.4% for AFI and BS; in the outer compartment, it was 19.5% for AFI and 17.9% for BS. In the case of DREAM, the higher B_1^+ inaccuracies caused a further distorted permittivity map (e.g., the rim around the phantom perimeter and mild spurious fluctuations in Figure 3D). In this case, average relative errors of 12% in the inner compartment and 35.4% in the outer compartment were observed, with peak errors up to 264% around the phantom perimeter. In general, the mean permittivity was offset from the input permittivity of ~6 units for both AFI and BS and of ~13 to 15 units for DREAM in both compartments (Table 3).

3.1.2 | Effect of transceive phase assumption

The effect of the transceive phase assumption on permittivity is illustrated in Supporting Information Figure S1 for our phantom. The transceive phase error ($\phi^{\pm}/2\text{-}\phi^{+}$; Supporting Information Figure S1A) appeared as left-right antisymmetry and was larger in the outer compartment, where the validity of the assumption degrades. The maximum error was 0.15 rad. A peripheral antisymmetric pattern was also reflected in the permittivity reconstructed with the transceive phase combined with the $|B_1^+|$ amplitude (Supporting Information Figure S1C). This led to a maximum bias of 15% with respect to the permittivity calculated based on the B_1^+ phase and amplitude. In general, using the transceive phase contributed mostly to the spread of permittivity values (Table 3). Similar effects have been observed for conductivity in previous studies.[28,62]

3.2 | Measurement results

Figure 4 presents the measurement results in the phantom for all B_1^+ methods. First, the SNR_1, namely the SNR of the first image (the highest in magnitude between the two signals), is shown. Second, the measured B_1^+ map is reported. Overall, each technique showed similar B_1^+ spatial distributions. Comparing B_1^+ maps from AFI and DREAM with respect to BS-based B_1^+ map resulted into differences of $<\pm 0.15$ rel. units, similar to the accuracy found in simulations (not shown). Third, maps for the std in B_1^+ ($\varsigma_{B_1^+}$) are shown, which were calculated from measured data as described in the Appendix. Despite its lowest SNR_1, DREAM introduced the smallest $\varsigma_{B_1^+}$ in the inner compartment (average $\varsigma_{B_1^+} = 4.3 \cdot 10^{-3}$ rel. units). BS had a slightly higher $\varsigma_{B_1^+}$ ($5.9 \cdot 10^{-3}$ rel. units), and AFI had almost two-fold $\varsigma_{B_1^+}$ ($1.1 \cdot 10^{-2}$ rel. units). In the outer compartment, the average $\varsigma_{B_1^+}$ for DREAM was slightly lower than for AFI ($3.5 \cdot 10^{-3}$ versus $4.9 \cdot 10^{-3}$ rel. units), but higher than BS ($\varsigma_{B_1^+} = 2.2 \cdot 10^{-3}$ rel. units). Finally, the corresponding permittivity maps are reported. Although affected by noise, BS- and DREAM-based permittivity maps displayed a bias pattern which resembles the permittivity reconstructions on simulated B_1^+ maps (Figure 3C): note, for instance, the rim of higher values and spurious fluctuations in the outer compartment periphery in DREAM-based permittivity. The measured permittivity mean values were, nonetheless, biased with respect to the values predicted with noisy simulations (~5 units in the outer compartment for all sequences and ~10, 2, and 8 units for AFI, BS, and DREAM, respectively, in the inner sphere). Also permittivity std

TABLE 3 Phantom permittivity (in relative units) obtained from simulations and measurements

	Simulations						Measurements	
	$\lvert B_1^+\rvert$ and B_1^+ phase (noiseless)		$\lvert B_1^+\rvert$ and transceive phase (noiseless)		$\lvert B_1^+\rvert$[a] and transceive phase		$\lvert B_+^1\rvert$ and transceive phase	
	Inner compartment	Outer compartment	Inner compartment	Outer compartment	Inner compartment	Outer compartment	Inner compartment	Outer compartment
TRUE[b]	80	36	80	36	80	36	80	36
INPUT[c]	80.64 ± 0.59	36.42 ± 0.76	80.45 ± 2.76	36.21 ± 5.94	—	—	—	—
AFI	74.69 ± 2.28	43.28 ± 3.46	74.49 ± 3.13	43.07 ± 6.66	73.79 ± 95.75	43.04 ± 26.14	83.77 ± 103.00	38.65 ± 31.85
BS	74.71 ± 2.26	42.74 ± 3.63	74.52 ± 3.11	42.52 ± 6.78	74.52 ± 44.02	42.57 ± 12.48	72.34 ± 47.65	38.40 ± 22.38
DREAM	65.02 ± 10.68	49.03 ± 13.86	64.81 ± 10.76	48.80 ± 14.86	63.52 ± 17.00	47.98 ± 28.93	56.87 ± 48.71	55.31 ± 46.69

Mean ± std values were calculated in 2 ROIs corresponding to both compartments. The boundary errors attributed to EPT reconstruction were excluded from the ROIs.
[a]Monte Carlo simulation to emulate the MR measurements. B_1^+ maps were affected by noise, which corrupted the original images I_1 and I_2.
[b]TRUE refers to the permittivity values measured with the dielectric probe and already reported in Table 1.
[c]INPUT refers to the permittivity values calculated from the input permittivity (i.e. the permittivity based on the input $|B_1^+|$ obtained directly from the EM simulation).

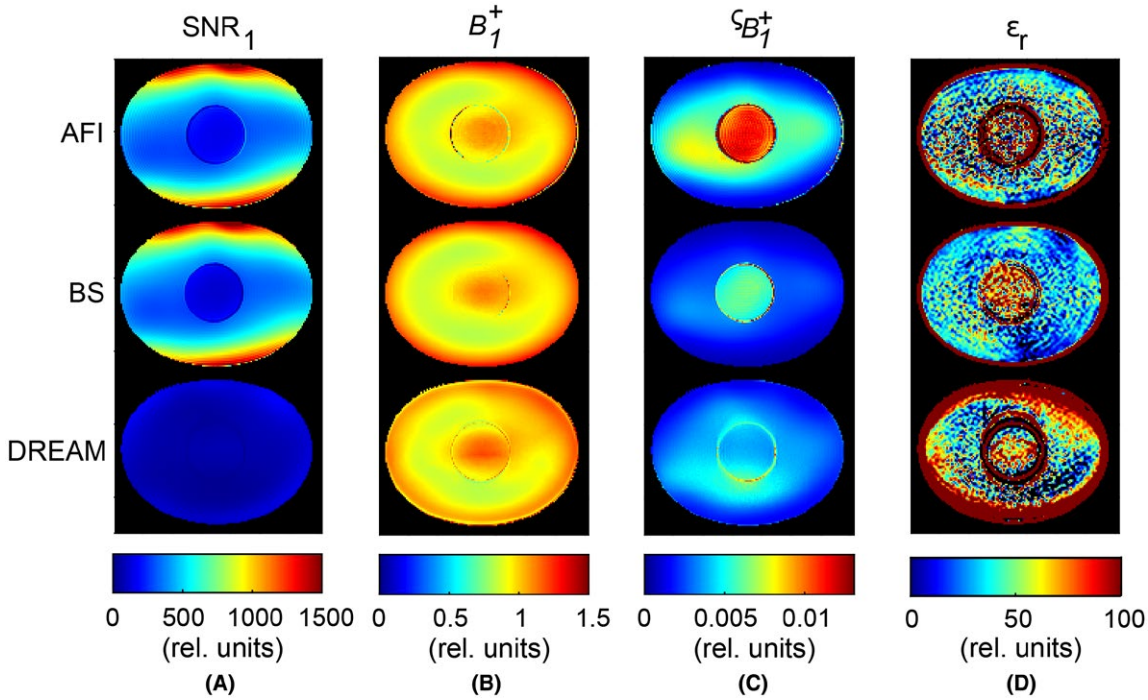

FIGURE 4 Phantom MR measurements. For each B_1^+ mapping technique (AFI, top row; BS, center row; DREAM, bottom row) the following maps are reported: A, SNR_1, namely the SNR relative to the image I_1; B, the B_1^+ field distribution. Values for the B_1^+ maps were normalized to the average value in the central slice; C, the B_1^+ standard deviation $\varsigma_{B_1^+}$, as calculated in the Appendix; and D, the permittivity ε_r

values were offset. These offsets were likely caused by experimental factors that were not simulated, such as ringing and ghosting due to fluid motion as a result of gradient switching.

Figure 5 presents in vivo results, which can be compared to the phantom results. In terms of B_1^+ precision (Figure 5C), the phantom inner sphere and the bladder were alike: the std in B_1^+ (average $\varsigma_{B_1^+} = 2.1 \cdot 10^{-2}$ rel. units) was considerably poorer in AFI than for the other two methods ($4.4 \cdot 10^{-3}$ and $5.1 \cdot 10^{-3}$ rel. units for BS and DREAM, respectively). With respect to the outer compartment, on average slightly lower $\varsigma_{B_1^+}$ values were measured in fat ($2.2 \cdot 10^{-3}$, $1.1 \cdot 10^{-3}$, and $4.0 \cdot 10^{-3}$ rel. units for AFI, BS, and DREAM, respectively). Overall, the $\varsigma_{B_1^+}$ averaged over the whole pelvis was $5.3 \cdot 10^{-3}$, $4.7 \cdot 10^{-3}$, and $5.1 \cdot 10^{-3}$ rel. units for AFI, BS, and DREAM. On the other hand, the measured B_1^+ maps (Figure 5B) exhibited different types of disturbances than the phantom measurements. AFI B_1^+ map was hampered by bowel motion. DREAM B_1^+ map showed sharp transitions at tissue interfaces (e.g., hip bone/muscle). In BS B_1^+ map, ghosting because of the flowing blood in iliac vessels appeared between hip bone and bladder. As expected, these disturbances were enhanced by the derivative kernel used for EPT reconstruction and generally corrupted the permittivity distribution. Nevertheless, the posterior part in BS-based permittivity map was unaffected by the abovementioned artifact. For the fat in that particular region, a permittivity of 5.3 ± 26.3 rel. units (mean ± std) was calculated, by excluding EPT boundary errors. The average value found was close to the literature value (5.9 rel.units[8]).

3.2.1 | Precision

In Figure 6, the relationship between the SNR_1 and $\varsigma_{B_1^+}$ is shown for the three sequences. In all cases, the simulated curves predicted the measured trends. The most favorable $\varsigma_{B_1^+}$- SNR_1 curve was found for DREAM, i.e. high B_1^+ precision was achieved for a relatively low image SNR. Note, however, that the measured SNR_1 range for DREAM was rather limited (measured max SNR_1 <350) in comparison to the SNR_1 obtained with AFI and BS (measured max SNR_1 >1000). Figure 6 also displays the asymptotic behavior of $\varsigma_{B_1^+}$, which implies that large jumps of image SNR would be necessary for rather small gains in B_1^+ precision.

Figure 7 illustrates our phantom experimental findings on the relationship between B_1^+ precision and permittivity precision. Also shown is the relationship for the EPT kernel used in this study, as theorized by Lee et al.[29] We found that BS achieved the smallest $\varsigma_{\varepsilon_r}$ in both compartments (22.4 and 47.6 rel. units in the inner and outer compartment, respectively) and that AFI-derived permittivity had the greatest $\varsigma_{\varepsilon_r}$ values (103.0 and 31.8 rel. units in the inner and outer compartments, respectively). Regarding DREAM, $\varsigma_{\varepsilon_r}$ was biased by the distorted permittivity distribution caused by sequence-related inaccuracies affecting the B_1^+ map.

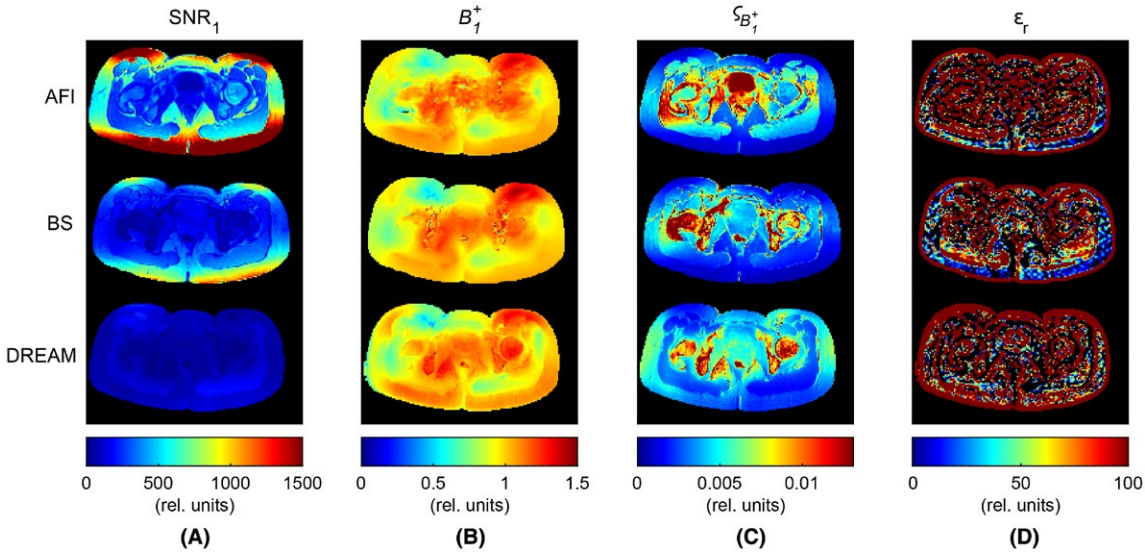

FIGURE 5 In vivo MR measurements on a female pelvis. For each B_1^+ mapping technique (AFI, top row; BS, center row; DREAM, bottom row) the following maps are reported: A, SNR_1, namely the SNR relative to the image I_1; B, the B_1^+ field distribution. Values for the B_1^+ maps were normalized to the average value in the central slice; C, the B_1^+ standard deviation $\varsigma_{B_1^+}$, as calculated in the Appendix; and D, the permittivity ε_r

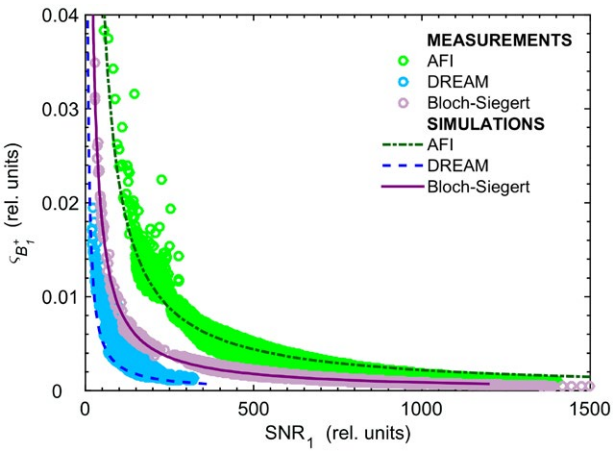

FIGURE 6 B_1^+ std (indicated by $\varsigma_{B_1^+}$) as a function of SNR_1, the SNR of the first image (I_1) for each technique, plotted for the central slice. The circles and lines represent the measured and simulated data, respectively. In simulations, different maps for SNR_1 and $\varsigma_{B_1^+}$, corresponding to different levels of ς_{noise}, were generated. For each ς_{noise}, SNR_1 and $\varsigma_{B_1^+}$ maps were averaged inside the phantom. The simulated trends shown in this figure are the result of the averaging operation. In the measured data, the voxels related to the plastic borders of both compartments were excluded. The simulated curves predicted well the behavior found in measurements

Overall, our results agreed well with Lee et al's theoretical model. Note that experimental factors, as mentioned earlier, might have slightly biased $\varsigma_{\varepsilon_r}$ values. Nonetheless, it is worth noticing that deviations of the same order of magnitude from the theoretical model were reported in the work by Lee et al[29] for an analytical complex B_1^+ map (i.e., no sequence dependence, transceive phase assumption, and experimental factors).

4 | DISCUSSION

We investigated, for the first time, the impact of B_1^+ acquisition on permittivity mapping. To this end, we designed a framework to predict and validate the sensitivity of the permittivity reconstruction to the sequence-specific accuracy and precision effectively achieved by the B_1^+ amplitude map at 3T. Moreover, we compared the accuracy and precision of Helmholtz-based permittivity maps reconstructed on B_1^+ maps measured with AFI, BS, and DREAM sequences. According to our definition, accuracy was associated with imperfections specific to the adopted sequence whereas precision (inverse of variance) was related to noise propagation. Our analysis demonstrated how the permittivity reconstruction is influenced by the sequence-specific error and noise propagation in the $|B_1^+|$ depending on which B_1^+ mapping sequence is used. More generally, we found that Helmholtz-based permittivity is extremely sensitive to both bias and noise in the B_1^+ map.

Regarding accuracy, BS- and AFI-based permittivity maps were comparably accurate in our phantom (Figures 3 and 4; Table 3). The B_1^+ maps from which these permittivity maps were reconstructed were also comparably accurate, which is in line with other studies.[58-60] DREAM-based permittivity, instead, deviated from the expected permittivity distribution because of inaccuracies in the B_1^+ map, which were larger at compartment interfaces. In vivo, permittivity maps were corrupted by under- and overshooting errors (also called "boundary errors") arising in correspondence of discontinuities in the B_1^+ distribution (Figure 5). These discontinuities manifested evidently at tissue interfaces in DREAM B_1^+ map and were likely caused by imperfect T_1 or T_2 decay of the stimulated echo.[55,69] Analogously,

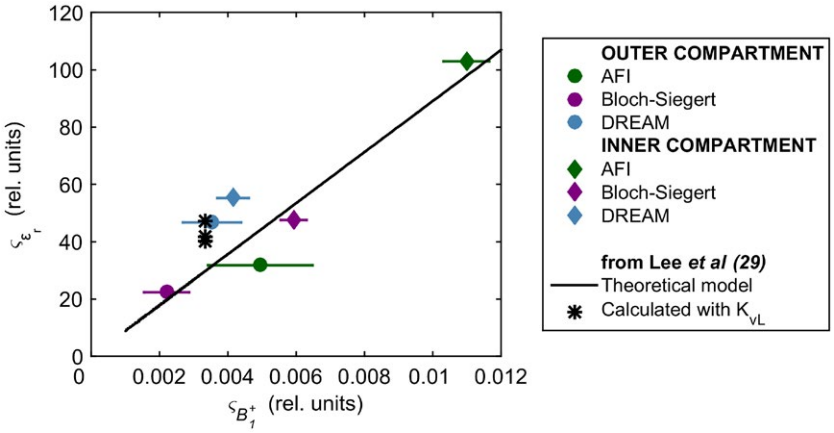

FIGURE 7 Experimental relationship between $\varsigma_{B_1^+}$ and $\varsigma_{\varepsilon_r}$. Both $\varsigma_{B_1^+}$ and $\varsigma_{\varepsilon_r}$ were evaluated in 2 manually delineated ROIs matching the phantom inner and outer compartments. For $\varsigma_{B_1^+}$, the average value is displayed. The horizontal bars indicate the spread (std) of the $\varsigma_{B_1^+}$ in both ROIs. The black line represents the theoretical model[29] relating $\varsigma_{\varepsilon_r}$ and $\varsigma_{B_1^+}$ for the noise-robust kernel K_{vL} (Equation 18 in Lee et al,[29] where $N_{tot} = 117$, $L = \sqrt{67}$, $G = 290.2$, and $\varsigma_{B_1^+} \approx 1/SNR_{B_1^+}$). The black asterisks refer to the std values of the permittivity calculated by Lee et al[29] inside 3 ROIs, for a simulated phantom B_1^+ map with fictitious $SNR_{B_1^+} = 300$

in vivo BS B_1^+ distributions were disturbed by ghosting artifacts due to sensitivity to flow, as a result of its "phase-based" B_1^+ encoding mechanism.[54]

Considering precision, we found that the permittivity std ($\varsigma_{\varepsilon_r}$) differed when the permittivity was derived from different B_1^+ sequences. For the most commonly used AFI technique, for example, the permittivity std was 1.5 to 2 times greater than for BS (Figure 7; Table 3). Note that, on average, the underlying std in B_1^+ ($\varsigma_{B_1^+} \approx \left(SNR_{B_1^+}\right)^{-1}$) for AFI was double the std in B_1^+ for BS. Similar findings on B_1^+ precision of AFI and BS were reported in previous works.[59,70] Although permittivity precision in the pelvis was not estimated because of the aforementioned boundary errors disturbing the permittivity map, the B_1^+ precision trends found in the phantom were also observed in the female pelvis, particularly in bladder, uterus, and fat (Figure 5). Thus, we expect the in vivo permittivity precision to be in the same order of magnitude as the phantom permittivity precision, because the noise propagation from the B_1^+ to Helmholtz-based permittivity is linear, as theoretically demonstrated by Lee et al.[29] Furthermore, by comparing the precision of the three sequences, our results experimentally validated Lee et al's theoretical model for the noise propagation from B_1^+ to permittivity (Figure 7).

Overall, extremely small errors in the B_1^+ map created considerable deviations in the permittivity distribution reconstructed with Helmholtz-based EPT. For example, BS results in the outer compartment showed that a less than 1% deviation in accuracy (or bias) in the simulated B_1^+ map (Figure 3B) resulted in 20% relative bias in permittivity (Figure 3D) and that a $\varsigma_{B_1^+} = 2.0 \cdot 10^{-3}$ rel. units, namely 0.2% of the average measured B_1^+, led to $\varsigma_{\varepsilon_r} = 22.4$ rel. units (Figure 7). In the pelvis, the std in B_1^+ measured, on average, 0.5% at 3T for all the sequences, with values as low as 0.1% in fat for BS and peaks higher than 2% in the bladder for AFI (Figure 5D). All these values, nevertheless, were far from the B_1^+ precision required to achieve $\varsigma_{\varepsilon_r} = 5$ units ($\varsigma_{B_1^+} \approx 0.05\%$; Figure 7), which we deem a considerable improvement for permittivity precision, in relation to the range of tissue permittivity (i.e., $20 \leq \varepsilon_r \leq 85$ rel. units for the majority of tissues at 128 MHz, except fat (see, e.g., studies[8,18-20])). Such a low std in B_1^+ would be reached only for image $SNR_1 \geq 2500$, 1500, and 500 rel. units for AFI, BS, and DREAM, respectively (Figure 6), but these SNRs were not achieved in our experimental setup (pelvis FOV in 5 minutes at 3T). Hence, we deduce that a Helmholtz-based approach cannot reconstruct precise permittivity maps for the B_1^+ precision clinically achieved by three commonly available sequences (at 3T for scan times ≤5 minutes).

Investigating more noise-robust solutions for permittivity mapping was beyond the scope of this study, but brain permittivity maps with superior quality were shown at 7T for Helmholtz-based EPT[51] and gEPT combined with multichannel systems.[37] Higher field strengths, in fact, benefit permittivity mapping not only for the intrinsic SNR gain, but also because the imprint of the displacement currents on the B_1^+ is stronger.[29,51] Moreover, improved permittivity results have very recently been reported by using newly formulated EPT reconstruction methods on B_1^+ maps from EM simulations. For example, using a quasi-Newton approach, Rahimov et al have shown a permittivity precision of ~20% in the brain.[39] In Guo et al, the std in permittivity, converted from the reported interquartile ranges according to the procedure in Wan et al,[71] was ~8 rel. units in white and gray matter and ~17 rel. units in cerebrospinal fluid.[41] In both studies, the simulated B_1^+ was directly corrupted with a noise level $\varsigma_{B_1^+} = 3.1 \cdot 10^{-3}$ (i.e., $SNR_{B_1^+} = 316$). Provided that these results are experimentally corroborated, using such less noise-sensitive EPT reconstruction methods or denoising techniques[52] could be preferred when precise permittivity maps obtained with clinical MR scanners (1.5 or 3T) are desired.

Our findings on accuracy also revealed that the slight perturbations of the B_1^+ field resulting from realistic permittivity variations (already studied in, e.g., Vaidya et al[25] and Brink et al[72]) can be in the same order of magnitude as the sequence-specific errors in the B_1^+ maps. Thus, although the severity of these errors on permittivity accuracy may vary depending on the chosen reconstruction technique and on the imaged body geometry, we conclude that using only electromagnetic simulations of the B_1^+ field is insufficient to fully investigate the accuracy of a permittivity reconstruction.

Despite the fact that our in vivo permittivity maps did not provide reliable quantitative estimates, we remark that we pragmatically tackled the unprecedented problem of assessing to what extent the B_1^+ acquisition influences the permittivity reconstruction. In light of all our results, we cannot give definitive solutions, but we can propose several directions for improvement, ranging from recommendations on sequence selection for permittivity mapping to suggestions on how to fully assess the quality of the reconstructed permittivity map. BS and AFI techniques should be preferred over DREAM for clinical applications where accurate permittivity estimates are of utmost importance, as is the case of hyperthermia treatment planning.[3] Strategies to mitigate some sequence-specific imperfections contaminating in vivo B_1^+ and permittivity distributions were beyond the scope of this study, but are worthy of further investigation (e.g., using flow compensation for BS or acceleration techniques to reduce motion artifacts for AFI). Alternatively, when precise reconstruction of the permittivity of certain tissues is desired, for example for tissue contrast visualization purposes, bear in mind that DREAM or BS had more favorable "B_1^+ precision-to-image SNR" performance than AFI. This recommendation is also valid when EPT algorithms prone to noise amplification (e.g., derivative-based methods) are used for permittivity reconstruction. Besides, if shorter scan durations are intended, then DREAM could allow the greatest time reduction (of ~3 minutes for our FOV), because of a higher flexibility in parameter settings; however, this might come at a cost of accuracy (e.g., by decreasing the shot interval length[69]) and loss of precision (e.g., by reducing the number of averages). More generally, to validate or predict the permittivity accuracy obtained with any new reconstruction method, or even to train a neural network,[73] we recommend taking the used B_1^+ mapping technique into account, for example by running Bloch simulations emulating the sequence, in addition to electromagnetic simulations of the B_1^+ field. Likewise, in order to predict or validate the method performance under clinically realistic noise levels valid for the majority of body tissues, we advise testing newly developed reconstruction methods against noise levels between 0.5% and 2.5% of the average B_1^+ (i.e., $40 \leq SNR_{B_1^+} \leq 200$).

5 | CONCLUSION

In conclusion, the merit of our work is to provide a methodology to assess the sensitivity of permittivity reconstruction to bias and noise in B_1^+ maps. Despite addressing only one reconstruction method and three B_1^+ mapping sequences, we emphasize that our framework, outlined in Figure 1, is reproducible for any type of B_1^+ mapping sequence (but also phase mapping sequence, if conductivity were of interest) and EPT reconstruction algorithm. By using this framework, two major findings were obtained. First, the B_1^+ mapping sequence affects the accuracy and precision of the permittivity reconstruction according to the sequence-specific error propagation determined by its B_1^+ encoding mechanism. This implies that attention should be paid to select the most appropriate B_1^+ mapping sequence in relation to the accuracy and precision desired in the final permittivity map. Second, the B_1^+ precision achieved by commonly available B_1^+ mapping techniques was below the precision needed to decrease the permittivity standard deviation to only 5 to 10 units, which means that the extreme sensitivity of Helmholtz-based EPT to noise perturbations, together with boundary errors, renders permittivity reconstruction not feasible at 3T in clinically acceptable times.

ORCID

Soraya Gavazzi https://orcid.org/0000-0003-4298-0353

REFERENCES

1. Katscher U, Voigt T, Findeklee C, Vernickel P, Nehrke K, Dössel O. Determination of electric conductivity and local SAR via B1 mapping. *IEEE Trans Med Imaging*. 2009;28:1365–1374.
2. Zhang X, Schmitter S, Van De Moortele PF, Liu J, He B, Bin He. From complex B1 mapping to local SAR estimation for human brain MR imaging using multi-channel transceiver coil at 7T. *IEEE Trans Med Imaging*. 2013;32:1058–1067.
3. van de Kamer JB, van Wieringen N, De Leeuw AA, Lagendijk JJW. The significance of accurate dielectric tissue data for hyperthermia. *Int J Hyperth*. 2001;17:123–142.
4. Kok HP, Kotte ANTJ, Crezee J. Planning, optimisation and evaluation of hyperthermia treatments. *Int J Hyperth*. 2017;33:593–607.
5. Hahn GM, Kernahan P, Martinez A, et al. Some heat transfer problems associated with heating by ultrasound, microwave or radio frequency. *Ann N Y Acad Sci*. 1980;335(1 Thermal Chara):327–346.
6. Crezee J, Bennis M, Gavazzi S, et al. Development of electrical properties tomography for hyperthermia treatment planning. In: 2017 First IEEE MTT-S International Microwave Bio Conference (IMBIOC). New York, NY: IEEE; 2017:1–4.
7. Balidemaj E, Kok HP, Schooneveldt G, et al. Hyperthermia treatment planning for cervical cancer patients based on electrical conductivity tissue properties acquired in vivo with EPT at 3 T MRI. *Int J Hyperthermia*. 2016;32:558–568.
8. Gabriel C. *Compilation of the Dielectric Properties of Body Tissues at RF and Microwave Frequencies*. San Antonio, TX: Air Force Materiel Command, Brooks Air Force Base; 1996.
9. Schepps JL, Foster KR. The UHF and microwave dielectric properties of normal and tumor tissues variation in dielectric properties with tissue water content. *Phys Med Biol*. 1980;25:1149–1159.

10. Rogers JA, Sheppard RJ, Grant EH, Bleehen NM, Honess DJ. The dielectric properties of normal and tumour mouse tissue between 50 MHz and 10 GHz. *Br J Radiol*. 1983;56:335–338.
11. Joines WT, Zhang Y, Li C, Jirtle RL. The measured electrical properties of normal and malignant human tissues from 50 to 900 MHz. *Med Phys*. 1994;21:547–550.
12. Lazebnik M, Popovic D, McCartney L, et al. A large-scale study of the ultrawideband microwave dielectric properties of normal, benign and malignant breast tissues obtained from cancer surgeries. *Phys Med Biol*. 2007;52:6093–6115.
13. O'Rourke AP, Lazebnik M, Bertram JM, Converse MC, Hagness SC, Webster JG, et al. Dielectric properties of human normal, malignant and cirrhotic liver tissue: In vivo and ex vivo measurements from 0.5 to 20 GHz using a precision open-ended coaxial probe. *Phys Med Biol*. 2007;52:4707–4719.
14. Gavazzi S, Limone P, De Rosa G, Molinari F, Vecchi G. Comparison of microwave dielectric properties of human normal, benign and malignant thyroid tissues obtained from surgeries: a preliminary study. *Biomed Phys Eng Express*. 2017;4:47003.
15. Halter RJ, Zhou T, Meaney PM, et al. The correlation of in vivo and ex vivo tissue dielectric properties to validate electromagnetic breast imaging: Initial clinical experience. *Physiol Meas*. 2009;30:S121–S136.
16. Shin J, Kim MJ, Lee J, et al. Initial study on in vivo conductivity mapping of breast cancer using MRI. *J Magn Reson Imaging*. 2015;42:371–378.
17. Tha KK, Katscher U, Yamaguchi S, et al. Noninvasive electrical conductivity measurement by MRI: a test of its validity and the electrical conductivity characteristics of glioma. *Eur Radiol*. 2018;28:348–355.
18. Wang H, He Y, Yan Q, et al. Correlation between the dielectric properties and biological activities of human ex vivo hepatic tissue. *Phys Med Biol*. 2015;60:2603–2617.
19. Schwan HP. Electrical properties of tissues and cell suspensions: mechanisms and models. In Proceedings of the 16th Annual International Conference of the IEEE Engineering in Medicine and Biology Society, Baltimore, MD, 1994. pp. 70–71.
20. Pethig R. Dielectric properties of biological materials: biophysical and medical applications. *IEEE Trans Electr Insul*. 1984;EI-19:;453–474.
21. Katscher U, van den Berg CAT. Electric properties tomography: biochemical, physical and technical background, evaluation and clinical applications. *NMR Biomed*. 2017;30:e3729.
22. Liu J, Wang Y, Katscher U, He B. Electrical properties tomography based on B1 maps in MRI: principles, applications, and challenges. *IEEE Trans Biomed Eng*. 2017;64:2515–2530.
23. Yang QX, Wang J, Zhang X, et al. Analysis of wave behavior in lossy dielectric samples at high field. *Magn Reson Med*. 2002;47:982–989.
24. Collins CM, Liu W, Schreiber W, Yang QX, Smith MB. Central brightening due to constructive interference with, without, and despite dielectric resonance. *J Magn Reson Imaging*. 2005;21:192–196.
25. Vaidya MV, Collins CM, Sodickson DK, Brown R, Wiggins GC, Lattanzi R. Dependence of B1− and B1+ field patterns of surface coils on the electrical properties of the sample and the MR operating frequency. *Concepts Magn Reson Part B Magn Reson Eng*. 2016;46:25–40.
26. Wen H. Noninvasive quantitative mapping of conductivity and dielectric distributions using RF wave propagation effects in high field MRI. In: Yaffe MJ, Antonuk LE, eds. *Proc SPIE 5030, Medical Imaging: Physics of Medical Imaging*. Bellingham, WA: International Society for Optics and Photonics; 2003:471–477.
27. Voigt T, Katscher U, Doessel O. Quantitative conductivity and permittivity imaging of the human brain using electric properties tomography. *Magn Reson Med*. 2011;66:456–466.
28. van Lier ALHMW, Brunner DO, Pruessmann KP, et al. B1+ phase mapping at 7 T and its application for in vivo electrical conductivity mapping. *Magn Reson Med*. 2012;67:552–561.
29. Lee SK, Bulumulla S, Hancu I. Theoretical investigation of random noise-limited signal-to-noise ratio in MR-based electrical properties tomography. *IEEE Trans Med Imaging*. 2015;34:2220–2232.
30. Zhang X, Zhu S, He B. Imaging electric properties of biological tissues by RF field mapping in MRI. *IEEE Trans Med Imaging*. 2010;29:474–481.
31. Yarnykh VL. Actual flip-angle imaging in the pulsed steady state: a method for rapid three-dimensional mapping of the transmitted radiofrequency field. *Magn Reson Med*. 2007;57:192–200.
32. Cunningham CH, Pauly JM, Nayak KS. Saturated double-angle method for rapid B1+ mapping. *Magn Reson Med*. 2006;55:1326–1333.
33. Bulumulla SB, Lee SK, Yeo DTB. Conductivity and permittivity imaging at 3.0T. *Concepts Magn Reson Part B Magn Reson Eng*. 2012;41B:13–21.
34. Sodickson DK, Deniz CM, Ben-Eliezer N, et al. Generalized local maxwell tomography for mapping of electrical property gradients and tensors. Proceedings of the 21st Annual Meeting of ISMRM, Salt Lake City, UT, 2013. p. 4175.
35. Hafalir FS, Oran OF, Gurler N, Ider YZ. Convection-reaction equation based magnetic resonance electrical properties tomography (cr-MREPT). *IEEE Trans Med Imaging*. 2014;33:777–793.
36. Balidemaj E, Van Den Berg CAT, Trinks J, et al. CSI-EPT: a contrast source inversion approach for improved MRI-based electric properties tomography. *IEEE Trans Med Imaging*. 2015;34: 1788–1796.
37. Liu J, Zhang X, Schmitter S, Van de Moortele PF, He B. Gradient-based electrical properties tomography (gEPT): a robust method for mapping electrical properties of biological tissues in vivo using magnetic resonance imaging. *Magn Reson Med*. 2015;74:634–646.
38. Serralles JEC, Daniel L, White JK, Sodickson DK, Lattanzi R, Polimeridis AG. Global maxwell tomography: a novel technique for electrical properties mapping based on MR measurements and volume integral equation formulations. In Proceedings of the 2016 IEEE International Symposium on Antennas and Propagation/USNC-URSI National Radio Science meeting, Fajardo, Puerto Rico, 2016. pp. 1395–1396.
39. Rahimov A, Litman A, Ferrand G. MRI-based electric properties tomography with a quasi-Newton approach. *Inverse Probl*. 2017;33: 105004. https://doi.org/10.1088/1361-6420/aa7ef2.
40. Liu C, Jin J, Guo L, et al. MR-based electrical property tomography using a modified finite difference scheme. *Phys Med Biol*. 2018;63:145013.
41. Guo L, Jin J, Liu C, Liu F, Crozier S. An efficient integral-based method for three-dimensional MR-EPT and the calculation of the RF-Coil-Induced Bzfield. *IEEE Trans Biomed Eng*. 2018;65:282–293.
42. Leijsen RL, Brink WM, van den Berg CAT, Webb AG, Remis RF. Three-dimensional contrast source inversion-electrical properties tomography. *IEEE Trans Med Imaging*. 2018;37:2080–2089.
43. Arduino A, Bottauscio O, Chiampi M, Zilberti L. Magnetic resonance-based imaging of human electric properties with phaseless contrast source inversion. *Inverse Probl*. 2018;34:084002.

44. Katscher U, Herrmann M, Amthor T, Findeklee C, Doneva M. Dictionary-based Electric Properties Tomography for brain conductivity imaging. In Proceedings for the 26th Annual Meeting of ISMRM, Paris, France, 2018. p. 5102.
45. Chung HJ, Kim JM, Jeong YJ, Kim JH, Lee C, Oh CH. Electromagnetic property mapping using Kalman filtering with a single acquistion at 3.0 T and 7.0 T MRI. In Proceedings for the 26th Annual Meeting of ISMRM, Paris, France, 2018. p. 5081.
46. van Lier ALHMW, Hoogduin JM, Polders DL, et al. Electrical conductivity imaging of brain tumours. In Proceedings of the 19th Annual Meeting of ISMRM, Montréal, Canada, 2011. p. 4464.
47. Voigt T, Väterlein O, Stehning C, Katscher U, Fiehler J. In vivo glioma characterization using MR conductivity imaging. In Proceedings of the 19th Annual Meeting of ISMRM, Montréal, Canada, 2011. p. 2865.
48. Huhndorf M, Stehning C, Rohr A, Helle M, Katscher U, Jansen O. Systematic brain tumor conductivity study with optimized EPT sequence and reconstruction algorithm. In Proceedings of the 21st Annual Meeting of ISMRM, Salt Lake City, UT, 2013. pp. 3626.
49. Katscher U, Abe H, Ivancevic MK, Keupp J. Investigating breast tumor malignancy with electric conductivity measurements. In Proceedings of the 23rd Annual Meeting of ISMRM, Toronto, Canada, 2015, p. 3306.
50. Balidemaj E, de Boer P, van Lier ALHMW, et al. vivo electric conductivity of cervical cancer patients based on B1+ maps at 3T MRI. *Phys Med Biol*. 2016;61:1596–1607.
51. van Lier ALHMW, Raaijmakers A, Voigt T, et al. Electrical properties tomography in the human brain at 1.5, 3, and 7T: a comparison study. *Magn Reson Med*. 2014;71:354–363.
52. Michel E, Hernandez D, Cho MH, Lee SY. Denoising of B_1^+ field maps for noise-robust image reconstruction in electrical properties tomography. *Med Phys*. 2014;41:102304.
53. Haacke EM, Brown RW, Thompson MR, Venkatesan R, eds. *Magnetic Resonance Imaging: Physical Principles and Sequence Design*, 1st edn. New York, NY: John Wiley & Sons; 1999.
54. Sacolick LI, Wiesinger F, Hancu I, Vogel MW. B1 mapping by Bloch-Siegert shift. *Magn Reson Med*. 2010;63:1315–1322.
55. Nehrke K, Börnert P. DREAM—a novel approach for robust, ultrafast, multislice B1 mapping. *Magn Reson Med*. 2012;68:1517–1526.
56. Morrell GR. A phase-sensitive method of flip angle mapping. *Magn Reson Med*. 2008;60:889–894.
57. Wade T, Rutt B. Comparison of current B1-mapping techniques. In Proceedings of the 15th Annual Meeting of ISMRM, Berlin, Germany, 2007. p. 354.
58. Morrell GR, Schabel MC. An analysis of the accuracy of magnetic resonance flip angle measurement methods. *Phys Med Biol*. 2010;55:6157–6174.
59. Pohmann R, Scheffler K. A theoretical and experimental comparison of different techniques for B1 mapping at very high fields. *NMR Biomed*. 2013;26:265–275.
60. Park DJ, Bangerter NK, Javed A, Kaggie J, Khalighi MM, Morrell GR. A statistical analysis of the Bloch-Siegert B1 mapping technique. *Phys Med Biol*. 2013;58:5673–5691.
61. De Greef M, Kok HP, Correia D, Borsboom PP, Bel A, Crezee J. Uncertainty in hyperthermia treatment planning: the need for robust system design. *Phys Med Biol*. 2011;56:3233–3250.
62. Balidemaj E, van Lier ALHMW, Crezee H, Nederveen AJ, Stalpers LJA, van den Berg CAT. Feasibility of electric property tomography of pelvic tumors at 3T. *Magn Reson Med*. 2015;73:1505–1513.
63. Voigt T, Homann H, Katscher U, Doessel O. Patient-individual local SAR determination: in vivo measurements and numerical validation. *Magn Reson Med*. 2012;68:1117–1126.
64. Van de Kamer JB, De Leeuw AA, Hornsleth SN, Kroeze H, Kotte AN, Lagendijk JJ. Development of a regional hyperthermia treatment planning system. *Int J Hyperthermia*. 2001;17:207–220.
65. Hargreaves B. Bloch Equation Simulator. http://mrsrl.stanford.edu/~brian/blochsim/.
66. Ku HH. Notes on the use of propagation of error formulas. *J Res Natl Bur Stand Sect C Eng Instrum*. 1966;70C:263.
67. Kellman P, McVeigh ER. Image reconstruction in SNR units: a general method for SNR measurement. *Magn Reson Med*. 2005;54:1439–1447.
68. Dietrich O, Raya JG, Reeder SB, Reiser MF, Schoenberg SO. Measurement of signal-to-noise ratios in MR images: influence of multichannel coils, parallel imaging, and reconstruction filters. *J Magn Reson Imaging*. 2007;26:375–385.
69. Nehrke K, Versluis MJ, Webb A, Börnert P. Volumetric B1+ mapping of the brain at 7T using DREAM. *Magn Reson Med*. 2014;71:246–256.
70. Khalighi MM, Sacolick LI, Rutt BK. Signal to noise ratio analysis of Bloch-Siegert B1+ mapping. In 18th Annual Meeting of ISMRM, Stockholm, Sweden, 2010. p. 2842.
71. Wan X, Wang W, Liu J, Tong T. Estimating the sample mean and standard deviation from the sample size, median, range and/or interquartile range. *BMC Med Res Methodol*. 2014;14:1–13.
72. Brink WM, Boernert P, Nehrke K, Webb AG. Ventricular B1+ perturbation at 7T—real effect or measurement artifact? *NMR Biomed*. 2014;27:617–620.
73. Mandija S, Meliadò EF, Huttinga NRF, Luijten PR, van den Berg CAT. Opening a new window on MR-based electrical properties tomography with deep learning. *arXiv*. arXiv:1804.00016 [physics.med-ph].
74. Haase A, Frahm J, Matthaei D, et al. MR imaging using stimulated echoes (STEAM). *Radiology*. 1986;160:787–790.

SUPPORTING INFORMATION

Additional supporting information may be found online in the Supporting Information section at the end of the article.

FIGURE S1 Effect of the transceive phase assumption on permittivity, for the phantom case. (a) Transceive phase error map, calculated as the difference between half of the transceive phase, $\phi^{\pm}/2$, and the transmit phase ϕ^{+}; (b) permittivity map reconstructed with the transmit phase; and (c) permittivity map reconstructed with the transceive phase. An antisymmetric pattern appears in the permittivity when the transceive phase assumption is used. In (b) and (c), the input B_1^+ amplitude map was used

How to cite this article: Gavazzi S, van den Berg CAT, Sbrizzi A, et al. Accuracy and precision of electrical permittivity mapping at 3T: the impact of three B_1^+ mapping techniques. *Magn Reson Med*. 2019;81:3628–3642. https://doi.org/10.1002/mrm.27675

APPENDIX: DERIVATION OF ERROR PROPAGATION (PRECISION) IN THE B_1^+, $\varsigma_{B_1^+}$

In each examined B_1^+ technique, two images, I_1 and I_2, are acquired. Their magnitude/phase representation is $I_1 = S_1 \exp(i\theta_1)$ and $I_2 = S_2 \exp(i\theta_2)$. Either the amplitudes or the phases of such images are then combined to form a B_1^+ map according to a sequence-specific function $f(x_1,x_2)$ where x_1 and x_2 are the input data (either magnitude or phase, depending on the mapping technique). In this section, a short summary and the sequence-specific function $f(x_1,x_2)$ are presented for each technique. Next, as a measure for precision, the std in the B_1^+ amplitude, $\varsigma_{B_1^+}$, for all the 3 methods is derived by applying the law of error propagation[66] (Equation A1):

$$\varsigma_{B_1^+} = \sqrt{\left(\frac{\partial B_1^+}{\partial x_1}\right) \cdot \varsigma_{x1} + \left(\frac{\partial B_1^+}{\partial x_2}\right) \cdot \varsigma_{x2}} \tag{A1}$$

where ς_{x_1} and ς_{x_2} are the standard deviations of the noise corresponding to, respectively, the signals x_1 and x_2.

Note that in the following expressions the B_1^+ represents the (dimensionless) spatial modulation of the transmit field, $B_1^+(\mathbf{r})$. Also known in literature as *transmit sensitivity*, $B_1^+(\mathbf{r})$ corresponds to the absolute B_1^+ field (in Tesla) normalized by the nominal B_1^+ value in T.

AFI

The AFI technique is a steady-state spoiled gradient-echo sequence with 2 interleaved repetition times TR_1 and TR_2 after an imaging pulse with constant nominal tip angle α_{nom}. Two images are acquired in each TR interval. Under the assumptions of perfect spoiling and repetition times shorter than T_1, the ratio of the magnitude images is related to the transmit field as follows[31] (Equation A2):

$$B_{1,AFI}^+(\mathbf{r}) = \frac{1}{\alpha_{nom}} \cdot \arccos\left(\frac{n\frac{S_2(\mathbf{r})}{S_1(\mathbf{r})} - 1}{n - \frac{S_2(\mathbf{r})}{S_1(\mathbf{r})}}\right) \tag{A2}$$

where $n = TR_1/TR_2$. Note that $x_1 = S_1$ and $x_2 = S_2$.

The expression for the B_1^+ std, $\varsigma_{B_1^+}$, is (Equation A3):

$$\zeta_{B_{1,AFI}^+} = \sqrt{\frac{1}{\alpha_{nom}^2} \cdot \frac{n^2-1}{(S_1^2 - S_2^2)(nS_1 - S_2)^2} \cdot (S_2^2 \cdot \zeta_{S_1}^2 + S_1^2 \cdot \zeta_{S_2}^2)} \tag{A3}$$

where ς_{S_i} is the std of the noise in the magnitude data. Note that this quantity is related to the SNR as $\zeta_{S_i} = \frac{S_i}{SNR_i}$, for $i = 1, 2$.

BS

The BS technique is a steady-state spoiled gradient echo sequence with an off-resonance pulse (in this case a Fermi pulse) inserted between the excitation and acquisition. The off-resonance pulse induces a B_1-dependent frequency shift, which is translated into a phase shift in the image. Acquiring 2 signals with opposite offset frequencies and subtracting their phase images leads to a phase shift difference that is related to the B_1^+ amplitude,[54] as expressed below (Equation A4):

$$B_{1,BS}^+(\mathbf{r}) = \frac{1}{A_{peak,Fermi}} \cdot \sqrt{\frac{\theta_1(\mathbf{r}) - \theta_2(\mathbf{r})}{2 \cdot K_{BS}}} \tag{A4}$$

with $x_1 = \theta_1$ and $x_2 = \theta_2$. $A_{peak,Fermi}$ is the Fermi pulse peak value. K_{BS} is a pulse-related constant that depends on the pulse waveform $B_{1,normalized}(t)$, its duration T_{Fermi} and its offset frequency ω_{Fermi}, as in Equation A5:

$$K_{BS} = \int_0^{T_{Fermi}} \frac{\left(\gamma \cdot B_{1,normalized}(t)\right)^2}{2\omega_{Fermi}} dt \tag{A5}$$

The std $\varsigma_{B_1^+}$ for BS is expressed by (Equation 6):

$$\zeta_{B_{1,BS}^+} = \sqrt{\frac{1}{8 \cdot \left(A_{peak,Fermi}\right)^2} \cdot \frac{\zeta_{\theta_1}^2 + \zeta_{\theta_2}^2}{K_{BS}(\theta_1 - \theta_2)}} \tag{A6}$$

where ς_{θ_i} is the std of the phase data θ_i, and is related to the image SNR by formula (15.84) in Haacke et al,[53] that is, $\varsigma_{\theta_i} = SNR_i^{-1}$ (radians), for $i = 1, 2$.

Note that Equation A6 coincides with Equation 20 of Pohmann and Scheffler[59] if $A_{peak,Fermi}$ is replaced by the expression of a (fictitious) block pulse with nominal flip angle α_{nom}, peak value $A_{peak,Fermi}$, and duration τ.

DREAM

In DREAM, a STEAM sequence,[74] is utilized to encode the B_1^+ information. The STEAM segment serves as a magnetization preparation before an imaging step composed by a train of RF pulses (also called shot) with gradient echo readout. A stimulated echo and a free-induction decay signals are acquired quasi-simultaneously in a single acquisition. The ratio

of their magnitudes ($x_1 = S_1$ and $x_2 = S_2$) is related to B_1^+ as indicated below[55] (Equation A7):

$$B_{1,DREAM}^{+}(\mathbf{r}) = \frac{1}{\alpha_{nom}} \cdot \arctan\left(\sqrt{\frac{2 \cdot S_1(\mathbf{r})}{S_2(\mathbf{r})}}\right) \quad \text{(A7)}$$

Applying Equation A1 for DREAM yields the following $\varsigma_{B_1^+}$ expression (Equation A8):

$$\zeta_{B_{1,DREAM}^{+}} = \sqrt{\frac{1}{\alpha_{nom}^2} \cdot \frac{1}{2(2S_1 - S_2)^2} \cdot \left(\frac{S_2}{S_1} \cdot \zeta_{S_1}^2 + \frac{S_1}{S_2} \cdot \zeta_{S_2}^2\right)} \quad \text{(A8)}$$

where ς_{S_i} is the std of the noise in the magnitude data and is related to the image SNR as $\zeta_{S_i} = \frac{S_i}{SNR_i}$, for $i = 1, 2$.